

## Fracture Toughness Measurements and Acoustic Emission Activity in Brittle Rocks

M. H. B. NASSERI,<sup>1</sup> B. MOHANTY,<sup>1</sup> and R. P. YOUNG<sup>1</sup>

*Abstract*—Fracture toughness measurements under static loading conditions have been carried out in Barre and Lac du Bonnet granites. An advanced AE technique has been adopted to monitor real-time crack initiation and propagation around the principal crack in these tests to understand the processes of brittle failure under tension and related characteristics of the resulting fracture process zone. The anisotropy of Mode I fracture toughness has been investigated along specific directions. Microcrack density and orientation analysis from thin section studies have shown these characteristics to be the primary cause of the observed variation in fracture toughness, which is seen to vary between  $1.14 \text{ MPa}\cdot(\text{m})^{1/2}$  and  $1.89 \text{ MPa}\cdot(\text{m})^{1/2}$  in Barre granite. The latter value represents the case in which the crack is propagated at right angles to the main set of microcracks. The creation of a significant fracture process zone surrounding the propagating main crack has been confirmed. Real-time imaging of the fracture process and formation of fracture process zone by AE techniques yielded results in very good agreement with those obtained by direct optical analysis.

**Key words:** Mode I fracture toughness anisotropy, acoustic emission, fracture process zone, microcrack density, microcrack orientation.

### 1. Introduction

Fracture toughness ( $K_{IC}$ ) of rocks, which is one of the basic material parameters in fracture mechanics, is defined as the resistance to crack propagation. It is considered an intrinsic material property that is finding increasing application in a number of fields such as stability analysis, hydraulic fracturing, rock fragmentation by blasting, and earthquake seismology. The uniqueness of the fracture toughness parameter applies to homogeneous and isotropic materials. For distinctly anisotropic or inhomogeneous conditions, that are characteristic of most common rocks, there may not be a unique value for this parameter. As a fracture property, it must depend on the nature of pre-existing microstructure in the rock that contributes to the latter's inhomogeneity. Among these are the extent and severity of microcracks and their

---

<sup>1</sup>Lassonde Institute, Department of Civil Engineering, University of Toronto, Toronto, ON, M5S 1A4, Canada. E-mail: bibhu.mohanty@utoronto.ca

alignment, and grain-size distribution; the boundaries among which can also be viewed as nascent microcracks.

To date, the role of microstructure on fracture toughness has been investigated strictly in terms of its global effect on the measured value of the latter. Scant attention has been paid to investigating the exact correlation between the two, especially where demonstrated fracture toughness anisotropy is concerned. The same applies to determining the interaction between microstructural properties and the propagating crack in the fracture toughness measurements. In the latter, the crack initiation point is predetermined as is the crack path. The interaction between these preexisting microcracks in the vicinity of the main propagating crack, and the possible formation of an extended fracture zone around the latter for example, are important considerations. The latter would essentially constitute the fracture process zone (FPZ) that may have significant bearing on foreshocks and aftershocks in earthquakes. Quantitative investigation of these phenomena and real-time monitoring of the fracture process by means of acoustic emission techniques constitute the essential goals of this study.

In a related investigation aimed at characterizing the microstructures and fracture toughness for a selection of granitic rocks, a very good correlation among microcrack density, microcrack length and fracture toughness has been demonstrated (NASSERI *et al.*, 2002, 2005a). This study further revealed that the combination of high microcrack density and microcrack length is responsible for lowering fracture toughness values. The average microcrack length shows a better correlation with fracture toughness than grain size in the rocks studied. It is evident from this study that fracture toughness is greatly influenced by microstructural properties of the subject rock. Mode I fracture toughness anisotropy as a function of layered microstructures in metals, alloys and composite materials has been investigated in the past (LI and XIAO, 1995; ENOKI and KISHI, 1995; KEVIN and BRIEN, 1998). LI and XIAO concluded that three main mechanisms, namely, weak interface cracking, fracture path deflection and delamination toughening, contribute to the strong anisotropy of Mode I fracture toughness for materials with layered microstructures. The effect of the anisotropic nature of coal on fracture toughness has also been studied both experimentally and analytically (KIRBY and MAZUR, 1985). The study concluded, as expected, that the fracture toughness was higher when measured orthogonal to bedding plane and was lowest for cracks propagating along the bedding plane.

The correlation between microcrack fabric in granitic rocks and anisotropy of physical properties such as seismic velocity, modulus, compressibility, uniaxial compressive and tensile strength, and fracture toughness has been studied by several authors (SANO *et al.*, 1992; TAKEMURA *et al.*, 2003). It has been reported that the orientation of physical anisotropy corresponded well with that of splitting planes in granites, (CHEN *et al.*, 1999). SCHEDL *et al.* (1986) upon studying Barre granite using optical SEM and TEM techniques, concluded that the splitting planes and anisotropy were mainly caused by microcracks.

In terms of real-time monitoring of the fracture process, the use of acoustic emission techniques (AE) has proven to be an excellent diagnostic tool. Extensive work has been done in laboratory and field locations using AE studies to understand fracture processes (LABUZ *et al.*, 1987; LOCKNER *et al.*, 1991; MOORE and LOCKNER, 1995; YOUNG and MARTIN, 1993; ZIETLOW and LABUZ, 1998; ZANG *et al.* 1998, 2000; LEI *et al.*, 2000; YOUNG *et al.*, 2004). The brittle fracture processes taking place at the grain size scale have a profound influence on the mechanical properties of rocks. The acoustic emission technique (AE) lends itself very well to studying this process in real time. The development of fast acquisition systems has enabled AE experiments to show fracture development under constant stress loading, thought to better approximate the low strain conditions in the Earth.

## 2. Fracture Toughness

The material property associated with the ability to carry loads or resist deformation in the presence of a crack is defined as the fracture toughness, ( $K_{IC}$ ). This parameter can be used to predict the nature of fracture onset depending upon the crack size and its sharpness (leading to the stress concentration effects), the stress level applied and the material property. The International Society for Rock Mechanics (ISRM) has recommended three methods, namely, Chevron Bend (CB), Short Rod (SR) and Chevron Cracked Notch Brazilian Disc (CCNBD) methods, (ISRM, 1988, 1995) for determining the fracture toughness of rock using core-based specimens. However, comparison tests among the three methods have consistently yielded 30 to 50% lower values with the CCNBD method than the other two (DWIVEDI *et al.*, 2000). This anomaly has been recently resolved, and suitable corrective procedures drawn up to yield fracture toughness values with CCNBD that are consistent with the other two methods (IQBAL and MOHANTY, 2005), provided special care is taken in the selection of specimen sizes and handling of anisotropy issues. The advantage of the CCNBD test method over the previous one is considered to be due to its easy adaptation to measuring fracture toughness anisotropy within one rock type. It requires much higher failure loads and exhibits reduced data scatter.

### 2.1 Chevron Cracked Notch Brazilian Disc (CCNBD) test

In this method (ISRM, 1995) the fracture toughness ( $K_{IC}$ ) is calculated by the following formula:

$$K_{IC} = \frac{P_{\max}}{B\sqrt{R}} Y_{\min}^* \quad (1)$$

where

$$Y_{\min}^* = \mu \cdot e^{\nu \cdot \alpha l} \quad (2)$$

$Y_{min}^*$  = critical dimensionless intensity value

$P_{max}$  = maximum load at failure

$B$  = thickness of the disc

$\mu$  and  $\nu$  are constants determined by  $\alpha_0, \alpha_B$ .

The geometry of the CCNBD is illustrated in Figure 1. The experimental parameters for Lac du Bonnet and Barre granites are given in Tables 1 and 2, respectively. All the dimensions of the geometry should be converted into dimensionless parameters with respect to specimen radius  $R$  and diameter  $D$ .

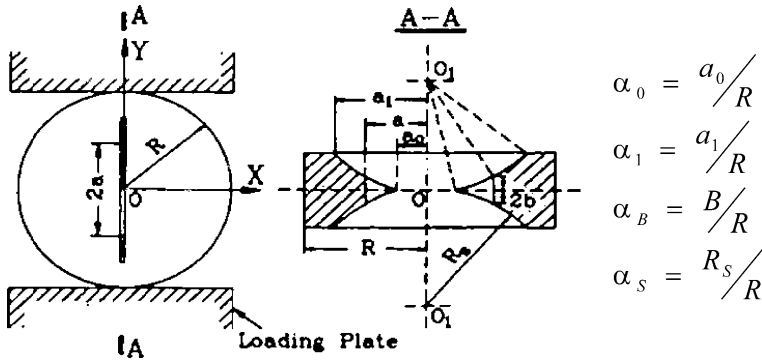


Figure 1  
Geometry of the CCNBD and related parameters (after ISRM, 1995).

Table 1

*CCNBD geometrical dimensions for Barre granite*

Descriptions	Values mm	Dimensionless expression
Diameter $D$ (mm)	75	
Thickness $B$ (mm)	30	$\alpha_B = B/R = \sim 0.79$
Initial crack length $a_0$ (mm)	8–9	$\alpha_0 = a_0/R = 0.21\text{--}0.25$
Final crack length $a_1$ (mm)	23.5	$\alpha_1 = a_1/R = \sim 0.62$
Saw diameter $D_s$ (mm),	50.0	$\alpha_S = D_s/D = 0.66$
$Y^*_{min}$ (dimensionless)	$\sim 0.78$	

Table 2

*CCNBD geometrical dimensions for Lac du Bonnet granite*

Descriptions	Values mm	Dimensionless expression
Diameter $D$ (mm)	194.8	
Thickness $B$ (mm)	51.10	$\alpha_B = B/R = 0.52$
Initial crack length $a_0$ (mm)	16.67	$\alpha_0 = a_0/R = 0.17$
Final crack length $a_1$ (mm)	56.08	$\alpha_1 = a_1/R = 0.575$
Saw diameter $D_s$ (mm),	147.4	$\alpha_S = D_s/D = 0.75$
$Y^*_{min}$ (dimensionless)	0.76	

### 3. Selection of Samples

In this study Barre and Lac du Bonnet granites were selected for studying the effect of microcrack orientation on fracture toughness and fracture growth process under Mode I fracture condition. These rocks are characterized by their preferred microcrack orientations and widely different grain size distribution.

#### 3.1 Microstructural Investigation

Microcrack observational techniques include 1) dye penetration prior to thin section preparation, 2) radiography and X-ray, 3) SEM and 4) TEM, (Kranz, 1983). In recent years the development of computer-aided image analysis programs has greatly facilitated microstructural characterization through analysis of digital images obtained from the thin sections (MOORE and LOCKNER, 1985; PRIKRYL, 2001; NASSERI *et al.*, 2005a). These new techniques are based on direct measurements of crack length through line tracing, and grain boundary tracing from thin sections. These methods provide easier handling of larger amount of data collected and therefore provide a more representative assessment of microstructural properties. The process in this study consisted of the following stages: Image acquisition from thin sections, image preprocessing, microcracks and grain boundary tracing, measurements with automated image analysis programs (LAUNEAU and ROBIN, 1996) and data analysis. A number of scan lines at fixed angular intervals is drawn which intercepts microcracks. The latter are converted to bitmap lineaments with a minimum width of four pixels (Fig. 2a). The total number of intercepts is converted to microcrack density and expressed as microcrack length per unite area with an appropriate scale (i.e., cm/pixel). A rose diagram is used to represent the overall orientation of the lineaments with respect to particular axes on the plane of interest (Fig. 2b).

##### 3.1.1 Microstructural characterization of Barre granite

Microstructural investigation in this study involved examination of thin sections along three orthogonal planes. Microstructural studies of this rock detailed the variation in terms of mineral size distribution, preferred microcrack orientation, microcrack density and microcrack length, measured along the three orthogonal planes. In our analysis one screen pixel represents 0.94  $\mu\text{m}$ . Thus the shortest resolvable crack and grain size has a cut-off limit of approximately 1  $\mu\text{m}$ . No attempt has been made in this study to measure the width of the microcracks, as some of them are finer than this cut-off limit. It has been shown that larger microcracks are the first to interact mechanically and thus dominate both the fracture process and the transport properties of rock (MADDEN, 1983; LOCKNER and MADDEN, 1991). Therefore limiting the observable crack and grain sizes to 1  $\mu\text{m}$  or larger should not be considered a drawback in the present investigation. Correlation of the rock's microfabric elements with the mechanical properties such as that of fracture

toughness requires knowledge of the original orientation of the rock or reference of orthogonal axis of the coordinate system (*X*, *Y* and *Z* axes) to the internal visible fabric of the rock. In the absence of any information regarding the natural *in situ*

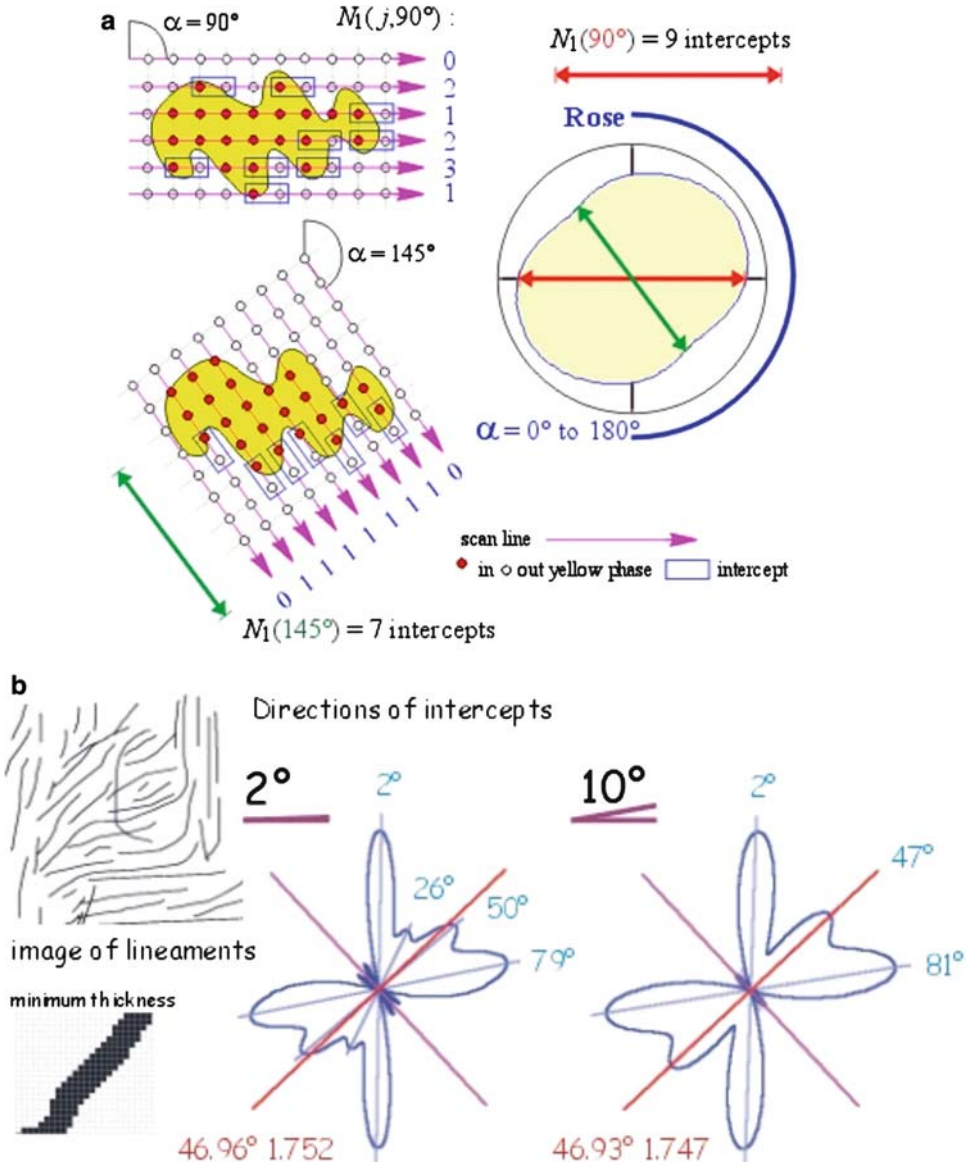


Figure 2

Illustration of scan lines intersecting a polygon or a lineament at different angular intervals (Fig. 2a), and rose diagram used to represent preferred orientation of lineaments with respect to particular axes on a plane of interest (Fig. 2b), (after LAUNEAU, P. and ROBIN, P-YF., 1996).

orientation of the granitic blocks and lack of visible internal rock fabric, thin sections were prepared normal to the three axes along which  $P$ -wave velocities were measured. Intermediate (3700 m/s) and slow (3300 m/s) and fast (4350 m/s) directions were assigned X, Y, and Z axes, respectively.

Barre granite is obtained from the southwest region of Burlington in the state of Vermont, USA. It is fine to medium grained rock with the mineral grain size ranging from 0.25 to 3 mm, with an average quartz grain size of 0.9 mm, which makes up 25% of this rock. The average feldspar grain size, the dominant mineral (70%), for this rock is 0.83 mm. The corresponding average biotite (6%) grain size in this rock is 0.43 mm. The microcracks are of intragranular type and are found in both the quartz, feldspar grains and along cleavage planes of biotite grains. The preferably oriented microcracks have an average length of 0.63 mm with maximum length of  $\sim 3.5$  mm cutting through the larger quartz grains observed in the YZ plane. It is evident from the 3-D block diagram of microcrack orientation in Figure 3, that the larger microcracks (2–3 mm long) are seen to run parallel to the Y axis and the shorter ones ( $\sim 1$  mm) run at higher angles to the Y axis and are parallel to the Z axis. In the XY plane, intermediate size microcracks ( $\sim 2$  mm) are oriented parallel to the Y axis and shorter ones are again parallel to the X axis in this plane. The longer

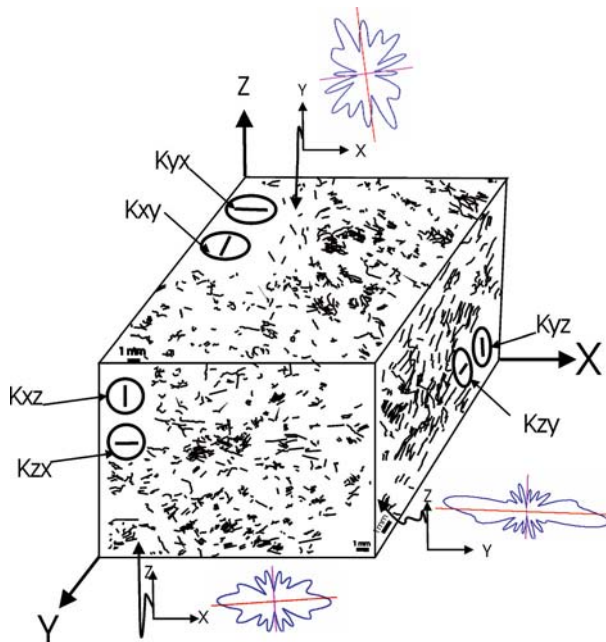


Figure 3

3-D block diagram showing location of CCNBD specimens prepared along each plane with respect to microcrack orientations in Barre granite; rose diagrams show the alignment of microcracks for each plane.

microcracks in the XZ plane are aligned parallel or at small angles to the X axis, whereas smaller microcracks are found to be parallel to the Z axis. The rose diagram representing the microcrack orientation and length along a certain direction for each plane is shown as well. Microcrack orientation analysis in Barre granite (Fig. 3) suggests a dominant alignment of pre-existing microcrack parallel to the XY plane. DOUGLASS and VOIGHT (1969) studied the microcracks orientation in Barre granite and demonstrated that a strong concentration of microcracks lies within the rift plane and the secondary concentration was found within the grain plane. XY plane is considered to be parallel to the rift plane and XZ parallel to the secondary concentration for Barre granite in this study.

### *3.2 Microstructural Characterization of Lac du Bonnet Granite*

This rock is medium to coarse grained with the mineral grain size ranging from 0.5 to 8 mm. The average grain size for this rock is about 3.5 mm and is composed of 60% feldspar, 30% quartz and 8% biotite. The microcracks are of an intragranular type and found in both quartz and feldspar grains. The average length of the microcracks is 4 mm with a maximum length of  $\sim 7$  mm. The rock sample is from the Underground Research Laboratory, Atomic Energy of Canada, where the concept of deep radioactive waste disposal is being studied.

### *3.3 Fracture Toughness Anisotropy and Microstructure*

The effect of microcrack orientation on fracture toughness of materials with layered microstructures and composites has been increasingly recognized as an important property. Similar investigations in rocks such as granite in which oriented microcracks have been found to be responsible for the splitting planes and anisotropy, help quantify the degree of anisotropy in otherwise isotropically and homogeneously treated rock. In the present study we use the CCNBD test method to evaluate this anisotropy in Barre granite. The Brazilian disk samples were prepared from three orthogonal planes with the notch orientation parallel to the main axis in each plane. The first index in CCNBD tests shown in Figure 3 represents the direction normal to the fracture plane, and the second index indicates the direction of crack propagation. The cracks were chosen to be parallel to one of the coordinate axes in this investigation and therefore CCNBD samples were prepared along six different directions with respect to microcrack orientation planes as shown in Figure 3.

Figure 4 illustrates the variation of fracture toughness measured along six different directions with the number of tests performed along each direction for Barre granite. Table 3 shows load at failure and calculated fracture toughness along six different directions including respective standard deviations, parallel to the axis of interest in three orthogonal planes. The average fracture toughness for the three fracture planes (i.e., YX, XY and YZ) reveal  $K_{IC}$  value of 1.9, 1.73 and 1.7



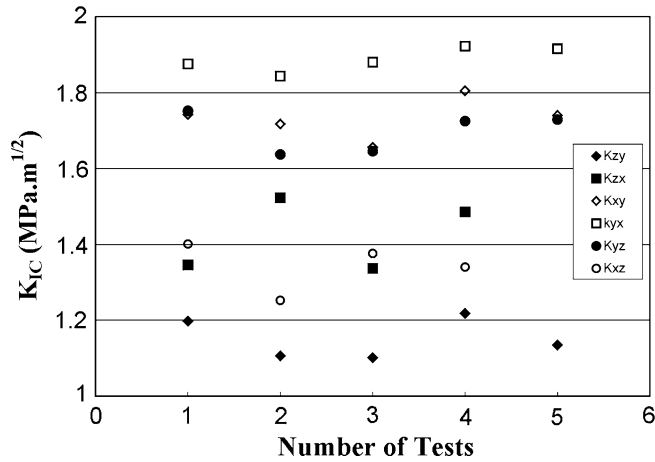


Figure 4

Variation of fracture toughness measured along six directions with the number of tests along each direction in Barre granite.

Table 3

Showing major mineralogical composition, measured load at failure and calculated fracture toughness along six different directions for Barre granite

Rock type	Quartz		Feldspar		Biotite		Load at failure kN Std. Dev.	K <sub>IC</sub> (MPa.m <sup>0.5</sup> ) Std. Dev.
	Av. grain % size (mm)		Av. grain % size (mm)		Av. grain % size (mm)			
XY Plane	0.93	25%	1.10	70%	0.46	4%	13 ± 0.46	{ K <sub>xy</sub> = 1.73 ± 0.06 K <sub>yx</sub> = 1.89 ± 0.03
							14.3 ± 0.16	
XZ Plane	0.95	23%	0.81	70%	0.43	6%	10.1 ± 0.54	{ K <sub>xz</sub> = 1.34 ± 0.07 K <sub>zx</sub> = 1.42 ± 0.1
							10.3 ± 0.7	
YZ Plane	0.94	26%	0.96	68%	0.40	4%	12.6 ± 0.42	{ K <sub>yz</sub> = 1.7 ± 0.05 K <sub>zy</sub> = 1.14 ± 0.05
							8.5 ± 0.4	

(MPa.m<sup>0.5</sup>), respectively, whereas the other three fracture planes XZ, ZX and ZY exhibit average K<sub>IC</sub> of 1.34, 1.42 and 1.14 (MPa.m<sup>0.5</sup>), respectively. It is noted that the first index in describing the fracture planes refers to the direction normal to the fracture plane and the second index refers to the direction of crack propagation or notch's tip direction.

It is ascertained that K<sub>IC</sub> measured along a direction normal to a pre-existing preferred microcrack plane (i.e., YX direction) is almost twice that measured in a parallel plane (i.e., ZY direction). Thin section studies and microcrack orientation analysis have been used to evaluate and explain these variations. Further analysis of morphology of the fracture forced to propagate along the direction that is

perpendicular to the microcrack plane shows increased segmentation, roughness and creation of wing cracks (Fig. 5). This is in sharp contrast to the fracture morphology of a crack propagating parallel to microcracks in Barre granite (Fig. 6), where it is seen to be relatively straight and free of any irregularities on the crack surfaces.

#### 4. Crack Propagation and Microstructure

##### 4.1 Fracture Process Zone

The fracture process zone (FPZ) in rocks is defined as the region affected by microcracking and frictional slip surrounding the visible crack tip propagating under stress, (LABUZ *et al.*, 1987; VERMILYE and SCHOLZ, 1999). The width of the FPZ is

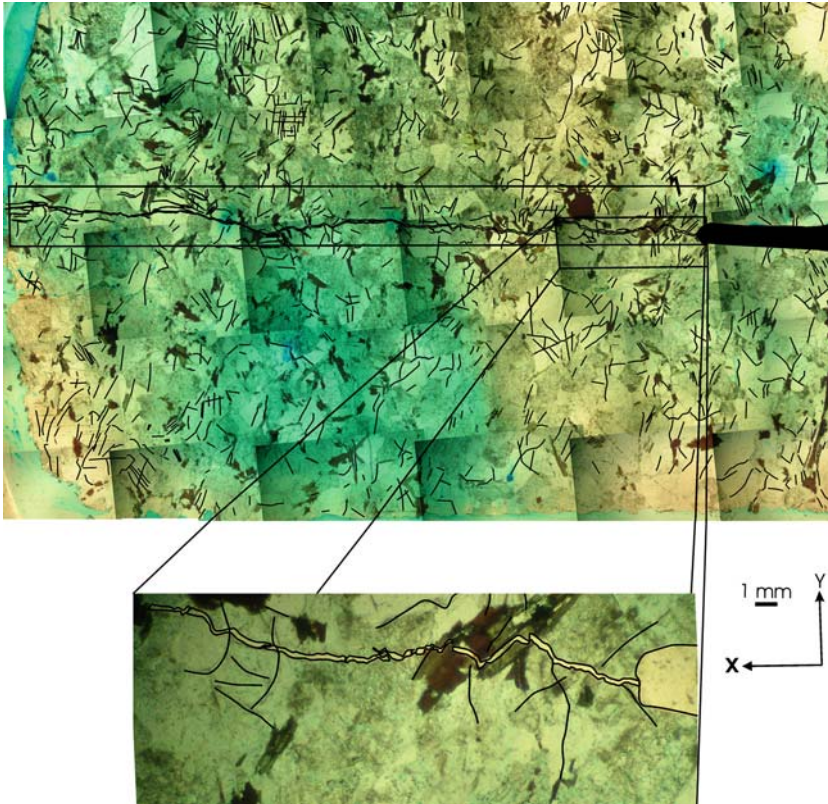


Figure 5

Fracture propagation (right side of image) normal to pre-existing preferably oriented microcracks in Barre granite. The close-up image shows the rough and segmented morphology of the fracture plane.

defined as the longest distance between visible cracks on either side of the main fracture and/or fault and its length is defined as the length between the fault tip and the crack with the greatest distance in front of the fault tip.

Dimensions of the fracture process zone (FPZ) based on the distribution of microcracks and acoustic emissions were investigated in various experimentally induced shear (LOCKNER, 1996; ZANG *et al.*, 2000) and tensile fractures (ZIETLOW and LABUZ, 1998). These studies suggest that in a FPZ microcrack, density and number of AE show an exponential decrease as a function of distance from the main failure plane. Similar observations are reported in the field based on meso and microstructural examinations across the faults plane (SCHOLZ *et al.*, 1993; WILSON *et al.*, 2003). It is observed that microcrack density increases by an order of magnitude in the FPZ surrounding the fracture tip in comparison with the



Figure 6

Fracture propagation (right side of the image) parallel to pre-existing preferably oriented microcracks in Barre granite. The close-up image shows the smooth morphology of the fracture plane. (The respective crack openings shown in close-up images in Figures 5 and 6 are not scaled and therefore, not comparable).

undamaged rock (NASSERI *et al.*, 2005b). In the present study the microcrack density profiles, as a function of distance on either side of the main fracture, have been taken as the basis for investigating FPZ. These are then compared with background or far-field microcrack density to delineate the width of the FPZ. Measurements of the longer transgranular microcracks on either side of the main fracture were used as additional guides. In this study an attempt is made to investigate the effect of oriented microcrack on FPZ width of Barre granite showing extreme values of fracture toughness. FPZ width analysis using a thin section technique for Lac du Bonnet granite for one plane is shown as well.

#### 4.1.1 Barre granite

Figure 7 shows the microcrack density ( $\Phi$ ) and microcrack orientation comparison between the far-field and FPZ in Barre granite for a situation in which the fracture is propagated from the notch's tip along a direction normal to microcracks. Figure 7 is the same as Figure 5 but with the grains removed from view. Microcrack orientation in the process zone is found to be parallel to the fracture propagation plane, and its density was observed to be almost twice that of the far-field microcrack density. FPZ width varies between 2 to 3 mm and maximum deviation of the fracture plane from the main propagation path is 1.26 mm, and this deviation increases towards the end of the 3.12-cm long fracture. Fracture deviation is measured with respect to the hypothetical fracture plane originating at the notch tip, had the fracture remained perfectly planar.

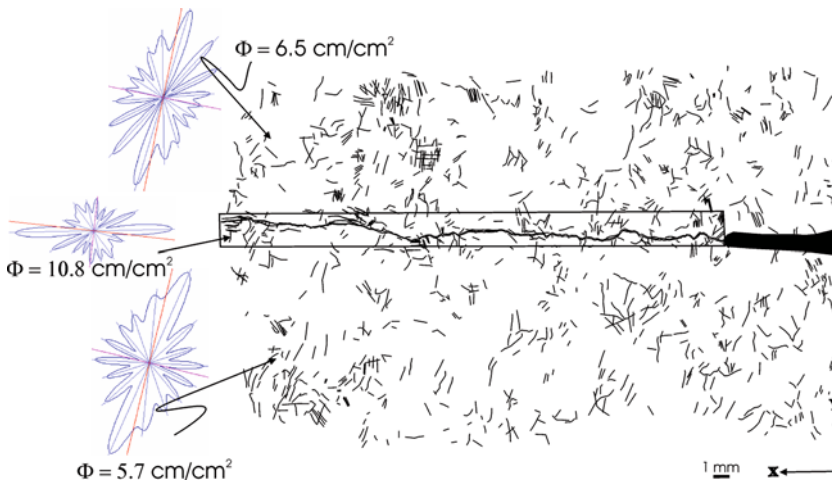


Figure 7

Microcrack density ( $\Phi$ ) and orientation (rose diagram) in the fracture process zone and far-field area in Barre granite (XY plane). Extended black box shows the width of FPZ.

Figure 8 shows the microcrack density and microcrack orientation comparison between the far-field and FPZ in Barre granite for a condition in which the fracture is directed parallel to microcracks. Figure 8 is the same as Figure 6, but with the grains removed from view. Microcrack density in the process zone is  $12.6 \text{ cm/cm}^2$  where far-field microcrack densities on either side of FPZ are  $6.7$  and  $4.5 \text{ cm/cm}^2$ . The rose diagram showing the microcrack orientations in FPZ, unlike that of the far-field ones, does not show slight maxima perpendicular to the main flat maxima running parallel to the main fracture. FPZ width in this direction is  $1.55$  to  $2 \text{ mm}$  and the maximum deviation of the fracture plane from the main propagation path is  $0.7 \text{ mm}$ . This deviation is observed mainly at the mid section of the  $2.85\text{-cm}$  long fracture.

#### 4.1.2 Lac du Bonnet granite

In this experiment, only one side of the directed crack issuing from the notch broke through the edge of the disc sample; the other end of the crack stopped just short of the edge of the sample. These are designated as notch A and notch B, respectively. Comparison of microcrack density and orientation between far-field and FPZ along YX plane and from the notch A side is shown in Figure 9. FPZ width for this rock is  $\sim 10 \text{ mm}$ . Microcrack density for far-field to FPZ varies from  $4.4 \text{ cm/cm}^2$  to  $10.7 \text{ cm/cm}^2$  and the rose diagram for the far-field area reveals several maxima parallel and normal to the fracture propagation direction. Whereas, the rose diagram for FPZ shows a single maxima parallel to the fracture direction. Figure 10 shows the microcrack density and the respective orientations measured in front of the arrested fracture (notch B) in Lac du Bonnet granite along the same plane. Microcrack density in front of the arrested tip reveals an order of magnitude increase in density ( $44 \text{ cm/cm}^2$ ) compared to far-field microcrack density. Microcrack orientations also reveal a sharp preferred direction in both FPZ and in front of the crack tip. These microfractures are also seen to be nearly parallel to the direction of crack propagation.

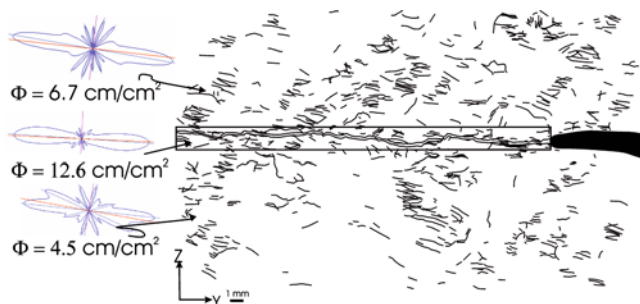


Figure 8

Microcrack density ( $\Phi$ ) and orientation (rose diagram) in the process zone and far-field area in Barre granite (YZ plane). Extended black box shows the width of FPZ.

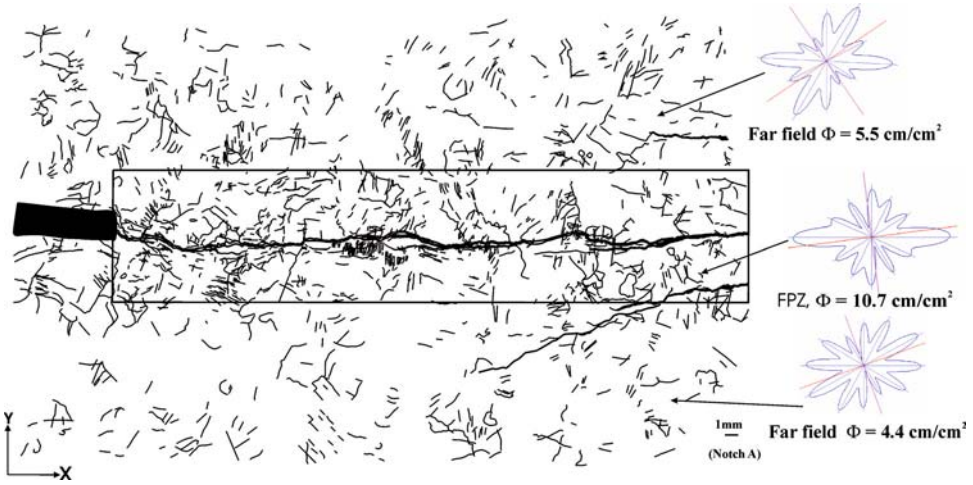


Figure 9

Microcrack density ( $\Phi$ ) and orientation (rose diagram) in the fracture process zone and far-field area in Lac du Bonnet granite (YX plane). Extended black box shows the width of the FPZ.

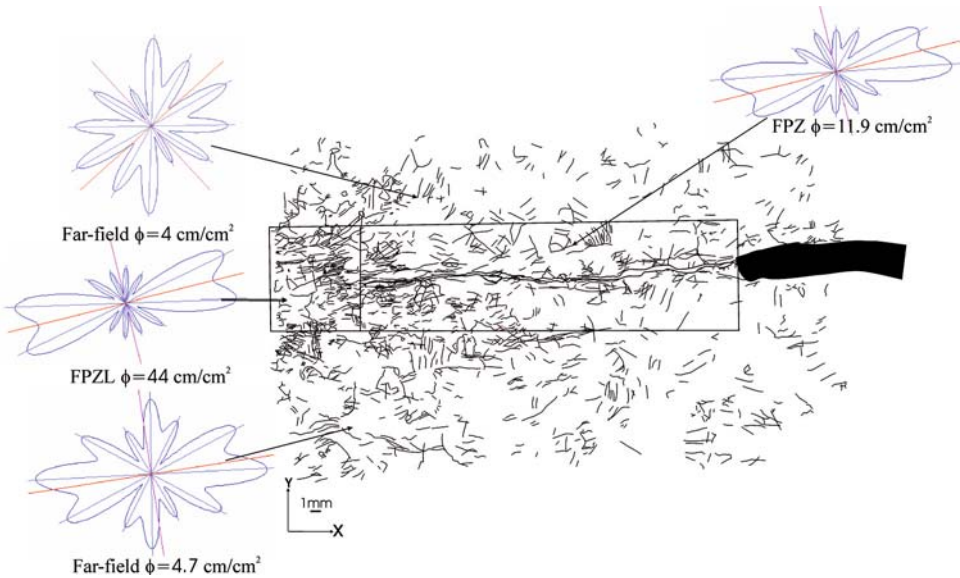


Figure 10

Microcrack density ( $\Phi$ ) and orientation (rose diagrams) in FPZ and far-field area in a seized fracture in notch B of Lac du Bonnet granite (YX plane). Extended black box shows the width of FPZ with the inset showing microcrack density ahead of arrested fracture.

## 5. *Acoustic Emission and Crack Propagation*

Both analytical and experimental AE studies have been carried out to demonstrate the usefulness of the former in core-based fracture toughness testing of rocks (HASHIDA, 1993). It has also been shown in plots of AE activity against time, that the steep rise of the former is representative of higher amplitude events than those generated at lower load levels (HASHIDA, 1993). Examination in thin sections of the test samples after the fracture toughness tests showed that the first region of the lower slope is associated with distributed microcracking around the notch tip, and that the steep slope corresponds to the localized macroscopic crack extension accompanied by the linking of microcracks.

The fracture toughness tests in Barre granite were carried out in 75-mm diameter samples. For reasons of assuring adequate precision in the location of acoustic emission events, detailed in the next section, considerably larger diameter samples are required. The AE portion of this study was therefore carried out in the Lac du Bonnet samples. The analogous nature of the fracture process in the two rock types, as demonstrated earlier, justified this selection. Except for scale, any conclusion based on the larger diameter samples should hold equally well in the smaller diameter sample with no loss of generality, especially for these two granitic rock types.

### 5.1 *Experimental Procedure*

#### 5.1.1 Experimental setup

In this study, the sample was line-loaded in a MTS loading machine, at a displacement rate of 0.0005 mm/s for testing of Lac du Bonnet granite. A considerably slower rate than suggested in ISRM (1995) was selected to facilitate microcrack development imaging using AE techniques. The displacement, force and time base of the experiment were controlled and recorded with TestStar software. The diagram of the CCNDD specimen and sensor locations are shown along two different planes in Figure 11a. Figure 11b shows the conceptual diagram of experimental setup used to record ultrasonic data.

AE events were captured using the Hyperion Giga RAM Recorder, which stores continuous ultrasonic waveform data onto a 40 GB circular Random Access Memory (RAM) buffer at 14-bit resolution. In this experiment, the sampling frequency was 10 MHz, providing a 134 second segment of continuous waveform data on 16 channels. The system functions as a continuous circular buffer that can be transferred to disk following the recording of a significant event. Advances in technology have lead to rapid AE waveform acquisition systems, allowing new observations of rupture. However, we believe this to be the first system to record continuous waveforms for significant time periods, thus removing the effect of 'mask' time, during which no AE are recorded while events are written to permanent storage and removing the sampling bias imposed by trigger levels. In addition to continuous

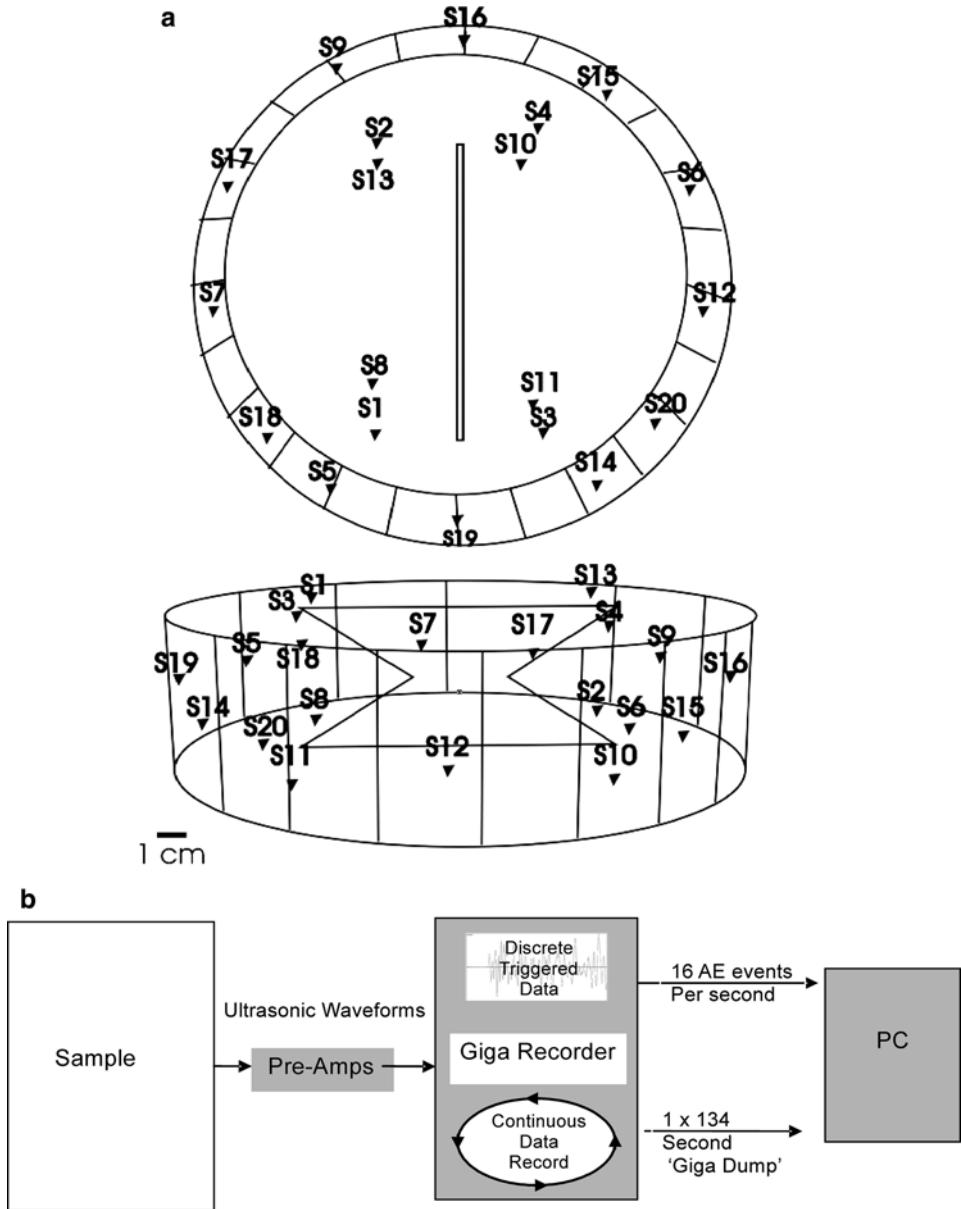


Figure 11

Schematic sketch of CCNBD specimen (Lac du Bonnet granite) and sensor locations on two different planes, (Fig. 11a) and experimental setup used for recording ultrasonic data (Fig. 11b).

data, the Giga RAM Recorder concurrently collects 'triggered' AE data during the entire experiment. Triggered data have identical recording parameters to continuous data. Each event has duration of 409.6  $\mu$ s, and a maximum of 16 events per second



are captured. The number of all AE counts per second is also recorded. The recorded ultrasonic signals passed through external 40 dB pre-amplifiers (PAC model 1220A). Four transmitters, dedicated as active sources for velocity surveys, were driven by a Panametrics 5072PR pulse generator module. The ultrasonic seismic velocity tests in the rock sample prior to notching exhibited anisotropic wave velocity behavior (Fig. 12), with the fast axis being 5290 m/s (AA' on Fig. 12) and the slow axis (EE' on Fig. 12) being 4550 m/s. The velocity anisotropy measurements were confined to prestressed conditions only, as such measurements during the actual loading process would have interfered with the accompanying acoustic emission events. The AE first arrivals were manually picked and source locations obtained using a Downhill Simplex algorithm (NELDER and MEAD, 1965), assuming a transversely anisotropy structure to an estimated accuracy of 3 mm. This necessitated the use of large diameter (195 mm) samples as mentioned earlier.

5.1.2 AE monitoring during crack initiation and propagation

Failure occurred 568 seconds after loading commenced, with the applied load reaching the peak value of 32.72 kN; the stress intensity factor  $K_I$  attains the highest value of 1.55 (MPa.m<sup>0.5</sup>) representing the fracture toughness,  $K_{IC}$  of Lac du Bonnet granite. A total displacement of 0.28 mm was recorded in this experiment. Approximately 1000 AE events were captured, for which the first arrivals were picked automatically. It was found that the presence of the notch caused complications, introducing location error. For the purpose of this paper, we present 355 manually processed AE events using an optimized array of 8 receivers for one of

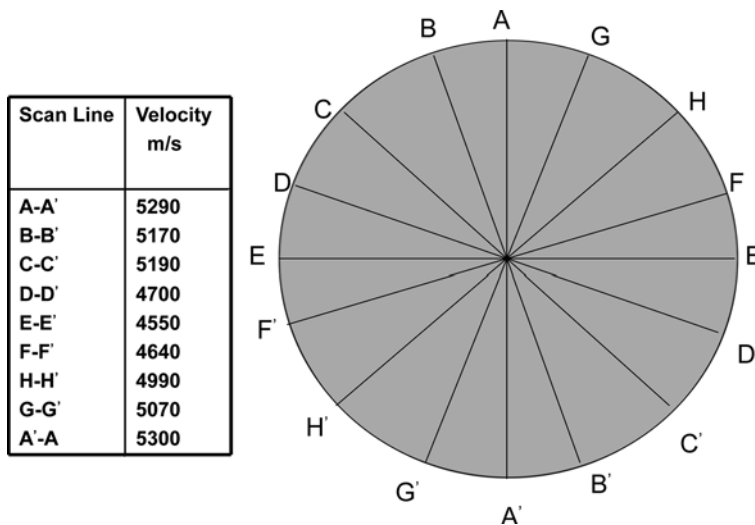


Figure 12  
Sensor locations and measured *P*-wave anisotropy in Lac du Bonnet granite.

the notches of the sample (notch A). Such a technique improves location accuracy greatly by removing the effects of the notch and increasing the accuracy of the first arrival picks. This improved location accuracy is important in comparison with microstructural observations.

The results from this test are shown in Figures 13a–d. Figure 13(a) shows AE hits per second, along with force versus time of loading. A plot of the cumulative number of AE events and stress intensity factor ( $K_I$ ) versus time is shown in Figure 13(b). The load versus displacement graph is shown in Figure 13(c). AE source locations are displayed from the final 17 seconds of the test, including post failure activity in Figure 14. These locations, divided into Stages A–E, are shown in Figure 13(d), which is an expansion of 13(a). AE locations are shown for each Stage as 1) discrete events, and 2) as a contour density plot. Views are shown along and perpendicular to the strike of the notch in Figure 14.

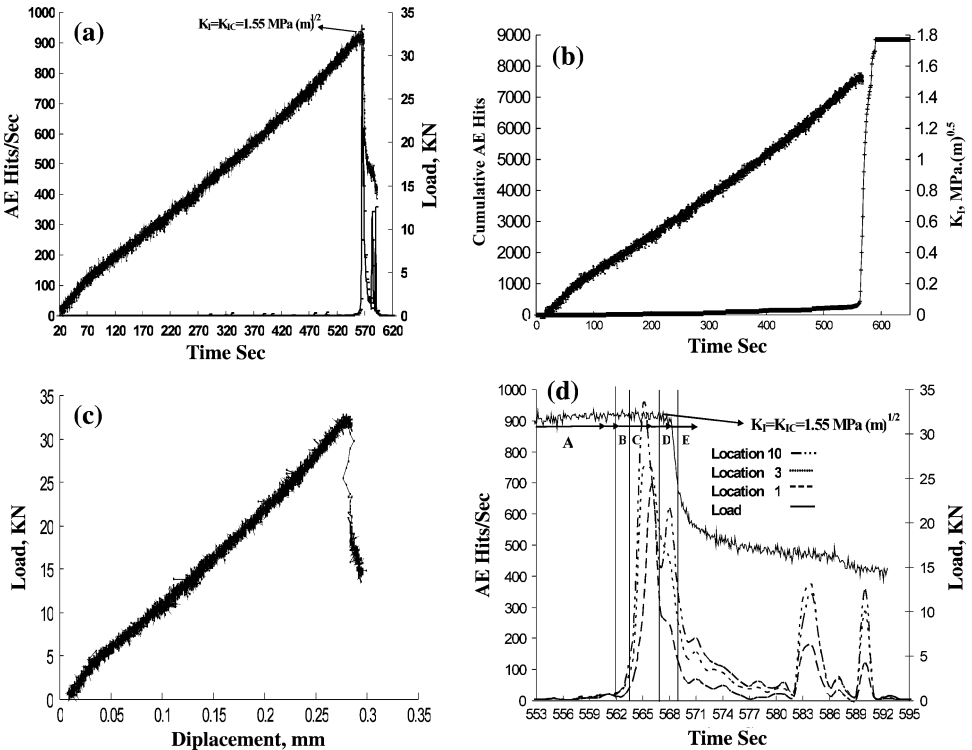


Figure 13

(a) Load and AE hits/second versus time (fracture toughness value for critical stress intensity factor is shown at top); (b) SIF ( $K_I$ ) and cumulative AE versus time; (c) Variation of load with displacement for CCNBD at failure; and (d) close-up window of load and AE hits (sensed at various locations ) versus time around fracture initiation and failure.

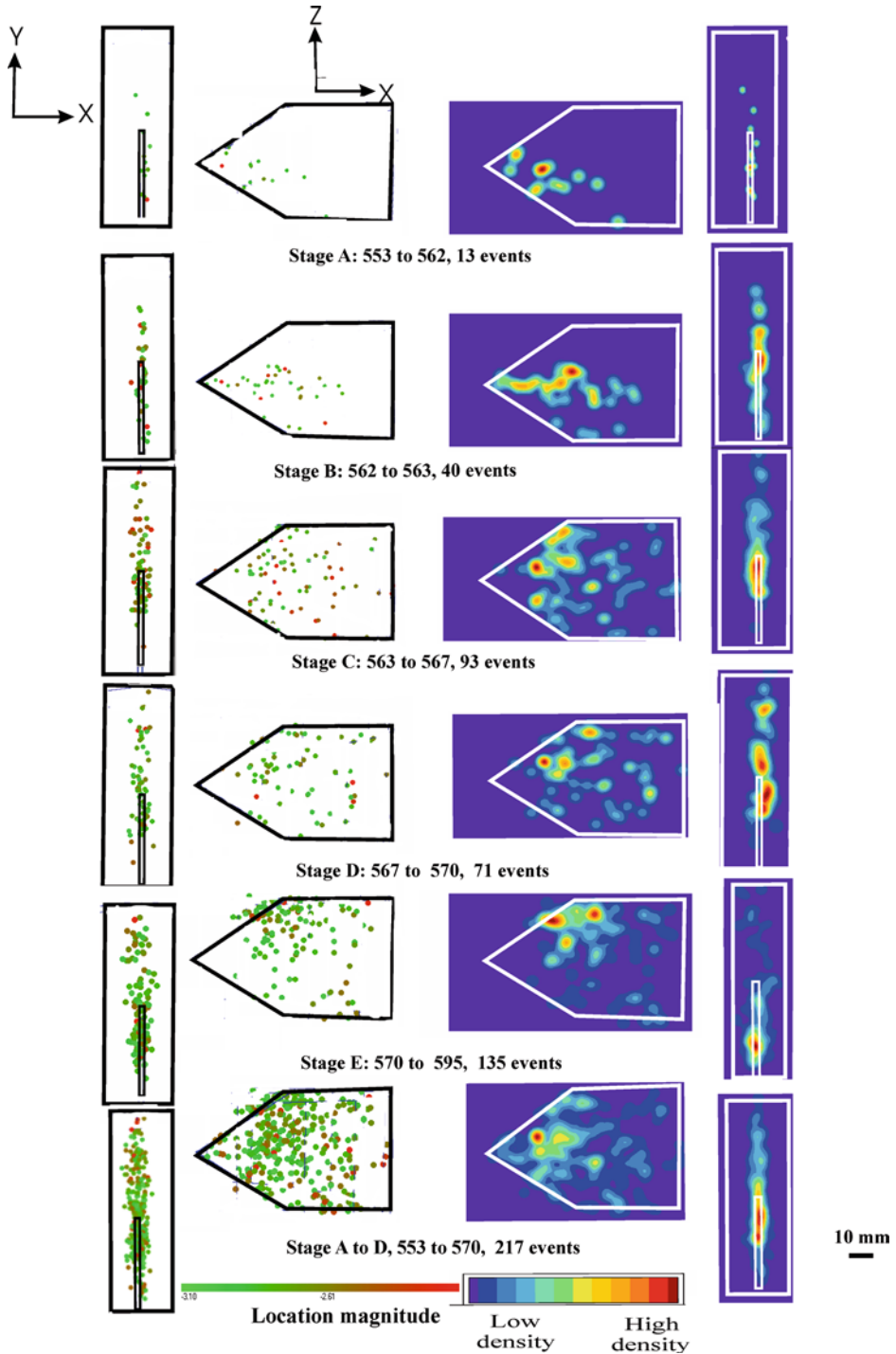


Figure 14

AE Source locations of 350 events (dots) and their equivalent density maps showing the final 17 seconds (Stages: A-D) in the experiment. Stage E shows the AE source location for post-failure region.

### 5.1.3 AE hypocenter distribution and fracture growth

*Stage A:* This stage corresponds to the recorded activity during nine seconds between 553 to 562 seconds, during which 13 events locate in the triangle defined by the notch region (this region is subsequently referred to as the notch triangle).

*Stage B:* In this two-second period, from 562 seconds to 563 seconds, there is a marked increase in AE event rate. Forty events are located in a narrow zone extending from the notch tip; the events mainly locating in the notch triangle.

*Stage C:* This period extended for four seconds, from 563 to 567 seconds, during which 93 AE events were located. However, the distribution becomes more planar, spreading through the notch-tip triangle to the edge of the sample. This could be interpreted as the fracture front extending, which would suggest a fracture propagation velocity of the order of cm/s. This applies to stable crack propagation in the region of the notch tip. There is insufficient event coverage to allow one to have a more specific figure on this velocity.

*Stage D:* This three-second period (567 to 570 seconds) contains 71 located events which have a similar location distribution to the previous stage. During this period, failure occurs starting between 568 and 569 seconds. The time interval from the rapid increase in AE rate (Stage B) to failure is 6 seconds.

*Stage E:* A twenty-one second period of post failure activity is shown during which 135 events locate mainly at the sample boundary within the notch triangle area.

The AE locations exhibit a change in distribution, whereby a linear feature is observed in Stage B, which progresses to a planar feature intersecting the sample boundary in Stage C. This could be interpreted as the fracture propagating two or three seconds before the sample fails. It is interesting to observe that locations are concentrated in the triangle defined by the notch, and comparatively few events are observed in the region where the fracture must propagate to cause failure. The reason for this change in the spread of the AE events is unclear at the moment.

## 5.2 AE Focal Mechanism Analysis

AE source mechanisms are calculated using a first motion polarity method (ZANG *et al.*, 1998). The polarity value of an event is calculated by:

$$Pol = \frac{1}{K} \sum_{l=1}^K \text{sign}(A_l^t), \quad (3)$$

where  $A$  is the first pulse amplitude and  $K$  is the number of channels used for hypocenter determination. For the transducers used in this test, compressional pulses arising out of tensile fractures are characterized with positive polarity. Events in the range  $0.25 < Pol \leq 1$  are defined as being tensile,  $-0.25 \leq Pol \leq 0.25$  are defined as shear and  $-0.25 \leq Pol \leq -1$  represent implosion or collapsed sources.

Analysis of 220 prefailure events revealed that 75% of the total events were of tensile type, 15% were of shear type and 10% had an implosion or collapsed source

type. For 134 post-failure events, 40% were shear type, 39% were tensile and 21% were implosion type.

Figure 15 demonstrates AE hits/sec and the load curve during the evolution of failure in Mode I. The percentage of AE events type versus time, between 562 to 569 seconds, i.e., six seconds before failure and last second (568th to 569th seconds) during failure in notch A (Fig. 15a) is shown. AE activity during 562 to 568 seconds increased from 3 to 45 events. These were predominantly tensile in nature. At the 567th second, of the 52 events recorded, 60% were tensile, 25% shear and 15% implosion type. A total of 42 events were recorded one second (i.e., 568th second) prior to failure or stress drop. During the failure between the times 568th to 569th

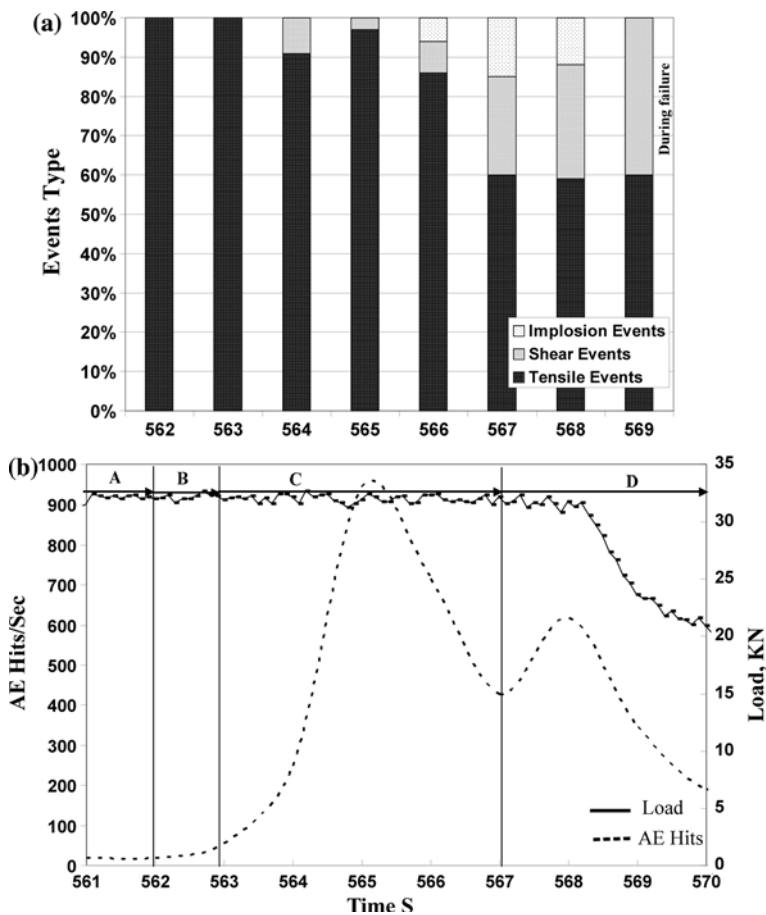


Figure 15

AE hits and the load curve during evolution of failure in Mode I. (a) Variation of event types (%) versus time at different stages of loading (A-D); (b) Variation of AE hits/sec versus time matched with the time in figure (a) to exhibit the relation between the event types (i.e., tensile, shear and implosion).

seconds, only ten events were recorded, in which 60% of the events were found to be of tensile and 40% proved to be of shear types. Variation of AE hits/sec versus time matched with time in Figure 15(a) is illustrated in Figure 15(b) to demonstrate the evolution of failure with time at various stages of loading and event types (i.e., tensile, shear and implosion).

## 6. Correlation of AE Technique with Optical Method

### 6.1 Microstructural Data from Notch A

A photo-mosaic showing the mineral fabric of notch A is presented in Figure 16; the notch being the black feature on the left side. The fracture plane resulting from this test is traced, and the microcracks are also marked. Superimposing AE source locations and optical images provides a unique opportunity to compare AE with microstructural observations. The lightly shaded region highlights the width of FPZ. For greater clarity, Figure 17 shows the same region with the mineral grains removed, to display only the fracture plane,

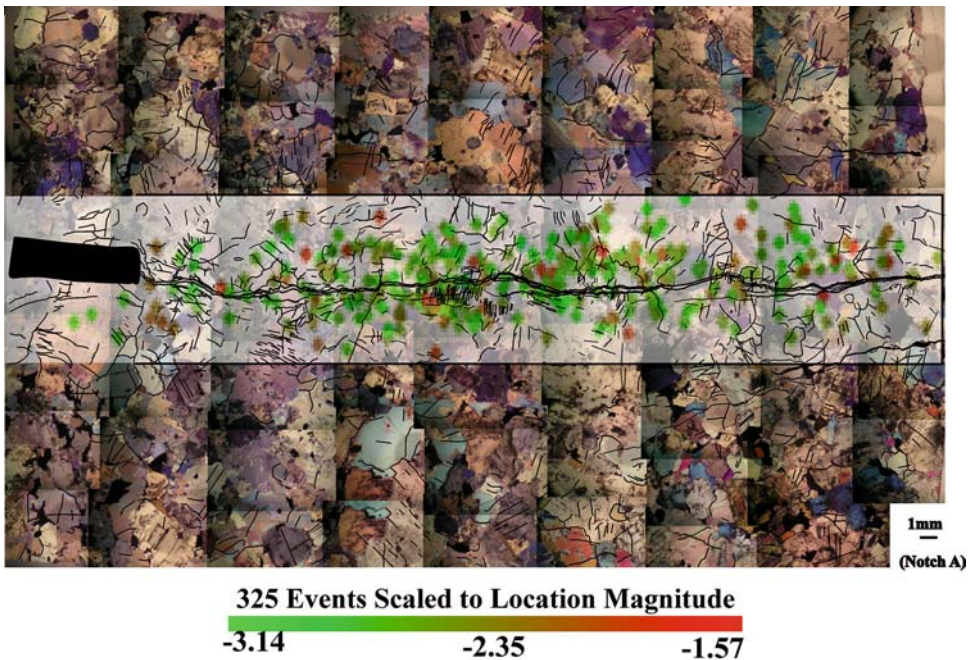


Figure 16

Tiled photo image of microstructure from thin section, around notch A (left side of image) with fracture trace and microcracks shown. 325 AE locations (dots) are superimposed.

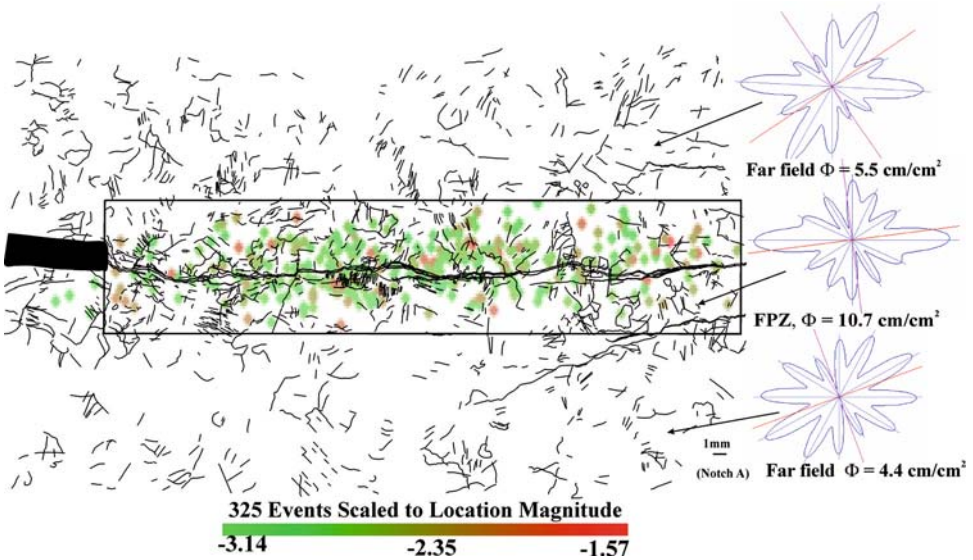


Figure 17

Microcrack density and orientation (rose diagram) in fracture process zone and far-field area in notch A. Inset delineates the width of FPZ as derived from the superimposed AE events.

microcracks and AE events. In addition, Figure 17 shows the microcrack density and orientation (see the rose diagrams). The density and orientation of the microcracks were systematically calculated for consecutive 2.5 mm wide zones, orientated parallel to the fracture trace. The length of the fracture is measured to be 85 mm; the FPZ width is optically estimated to be 10–15 mm, which matches well with the width determined using AE techniques.

### 6.2 Comparison of AE and Optical Observations of the FPZ

Figure 18 is a comparison of microcrack density obtained from microstructural analysis, and AE source location density plotted against distance from the macro-fracture trace for notch A. The AE density was calculated equivalent to the microcrack density. For both the AE and microstructural densities, there is an exponential increase in density towards the fracture. The FPZ widths inferred from both AE and optical measurements are closely correlated. This is at variance with earlier work (JANSSEN *et al.*, 2001) in which the FPZ resolution defined by AE was 2–4 times greater than the optical measurements. This discrepancy between these two studies could possibly be due to the fact that in the latter the width of FPZ would statistically represent the entire population of cracks and therefore be less dependent on some particular crack propagating under Mode I, as in the present study.

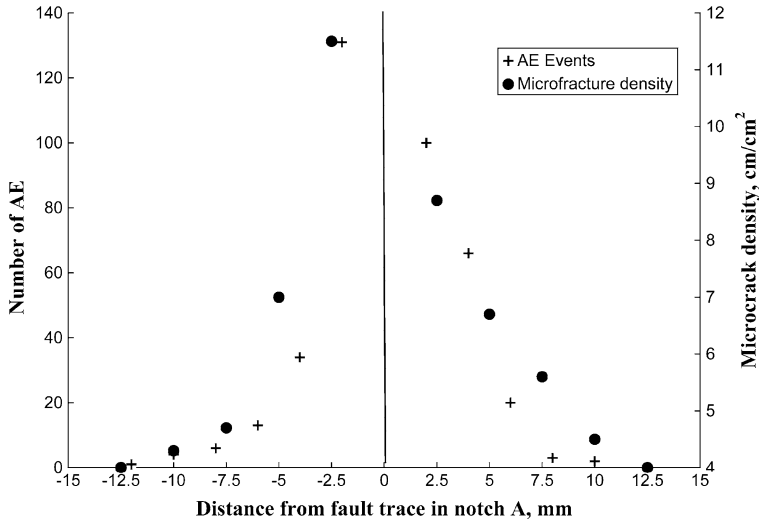


Figure 18

Correlation of AE events distribution with that of microcrack density as a function of distance from the fracture plane.

### 7. Discussions

The highest measured fracture toughness value i.e.,  $K_{IC} = 1.92$  (MPa.m<sup>0.5</sup>) in Barre granite was observed to be along the X direction in ZX plane ( $K_{yx}$ , fracture plane), which is normal to the direction of the main set of oriented microcracks (i.e., XY plane). The lowest value of 1.1 (MPa.m<sup>0.5</sup>) is found to be along the Y direction in XY plane ( $K_{zy}$ , fracture plane) where the fracture is propagated parallel to the Y direction in that plane along which delamination is easier. Two other planes with relatively higher average values i.e., 1.7 (MPa.m<sup>0.5</sup>) were observed to be along directions that are normal to two orthogonal sets of pre-existing microcrack planes. The other remaining two directions (i.e., X and Z in YX and YZ planes) with average  $K_{IC}$  of 1.42 and 1.34 (MPa.m<sup>0.5</sup>), respectively indicate the intermediate fracture toughness values for Barre granite. The crack propagation in the former direction is normal to YZ plane but parallel to YX plane. In the latter direction (in Z) the fracture is forced to propagate parallel to YZ and normal to XY planes. It is noted that the first index in describing the fracture planes refers to the direction normal to the fracture plane and the second index refers to the direction of crack propagation.

Further analysis of morphology of the fracture forced to propagate perpendicular to the microcrack plane also shows increased segmentation, roughness and creation of wing cracks (Fig. 5). This is in sharp contrast to the fracture morphology of a crack propagating parallel to microcracks in Barre granite (Fig. 6). This probably resulted in the different features associated with fracture process zone (FPZ), i.e., width and length of FPZ even within the same rock type. The width of the FPZ



measured on ZY (lowest  $K_{IC}$ ) plane ( $K_{zy}$ , fracture plane) is  $\sim 1.55$  to 2 mm and the maximum deviation of the fracture from the main path is 0.7 mm, whereas the width of FPZ measured on XY (highest  $K_{IC}$ ) plane ( $K_{yx}$ , fracture plane) is 2.2 to 3 mm and the maximum deviation of the fracture from the main path is 1.26 mm. Microcrack orientation analysis of the far-field and FPZ in both the planes characterized with extreme  $K_{IC}$  values shows that within the width of the FPZ microcracks are parallel to the main fracture irrespective of the orientation of the microcracks with respect to propagation direction. However, it should be pointed out here that all reference axes in the experiments with test samples were assigned on the basis of measured  $P$ -wave velocities along three arbitrarily fixed orthogonal axes. Therefore, these directions may not necessarily represent the maxima or minima of the characteristics studied in the test rocks as whole.

Stress interaction between a fracture and a field of microcracks (or process zone) generate irregular fracture propagation front, which is generally referred to as rugosity front (the fracture does not propagate like a straight razor blade for instance, but more or less like a rugous wavefront). Considering the stress intensity factors in Modes II and III, the asymmetrical microcrack field generates stress perturbations in modes II and III, although the main fracture is loaded in Mode I. Consequently, stress perturbations in Modes II and III, when large enough (e.g., in XY plane, Fig. 5) can promote out of plane fracture propagation (KACHANOV, 1994).

In terms of AE activity, it is seen that the AE rate rapidly accelerates a few seconds before failure. Source locations suggest a migration of a fracture plane could be occurring, mainly in the triangular area defined by the notch. The velocity of this fracture growth would be of order cm/s. The lack of AE locations between this area and the loading platen, through which region the fracture must propagate, could be due to a bias in the sensor array geometry, preventing accurate locations in this area. It is also observed that the initial linear alignment of AE events near the notch tip spreads out to a more planar configuration, with major events aligned perpendicular to the propagation direction of the notch tip. The reasons for these observations are the subject of a continuing investigation. The majority of prefailure AE events are interpreted as tensile, whereas postfailure, an equal number (40%) are interpreted as due to shear and tensile fractures. This change in mechanism could be synonymous with movement of a fault plane accompanied by shearing of asperities. Focal mechanism analysis based on first motion results of shear failure experiments reveals the preponderance of quadrant type (double couple) and complex type events over tensile type events (reviewed by LOCKNER, 1993). Analysis of the first motion results of the events in the present study demonstrate the early predominance of tensile type events (85% to 97%) due to the nature of the test itself, changes to less dominantly tensile events (60%) compared to shear-type events (40%), 2~3 seconds prior to failure (Fig. 15). Generation of rugosity front can be equated with the creation of stress intensity factor in Modes II and III, as a result of stress interaction between the main fracture and the pre-existing field of microcracks.

A delay on the order of three seconds between failure of the sample (pick load drop) and peak AE activity has been noted. Similar observations have been made by previous researchers (LEI *et al.*, 2000). This could possibly be due to the decrease in the number of AE events that are recognized as separate events; for example, because of overlapping of AE events before failure. Analysis of cumulative AE energy during that instant could be useful for such clarification, which is a part of continuing research.

Microstructures analysis demonstrates that the width of the FPZ is between 10 and 15 mm while the fracture length is only 85 mm in Lac du Bonnet granite. In the FPZ, microcrack density is around  $11 \text{ cm/cm}^2$ , while the far-field background value is approximately  $4 \text{ cm/cm}^2$ . However, in front of an arrested fracture, the microcrack density reaches  $44 \text{ cm/cm}^2$  which is consistent with theoretical investigations on the fractal nature of newly created fracture surfaces in brittle materials (CHELIDZE *et al.*, 1994). Similarly, the microcrack orientation is found to have a dominant plane in the FPZ, whereas in the far-field no dominant orientation is observed. Unlike previous studies, we find that both AE activities and microcrack densities increase exponentially towards the fracture plane. The two approaches also yield the same FPZ width, which suggests that the AE approach can be used as a diagnostic tool to investigate the formation of FPZ related to Mode I tests.

## 8. Conclusions

A systematic laboratory study involving tensile loading of homogeneous granitic rocks (Mode I fracture) under standard test procedures (i.e., Cracked-Chevron-Notch-Brazilian-Disc) and an advanced acoustic emission system (AE) has been carried out with Barre and Lac du Bonnet granitic samples. It was shown that the measured value of fracture toughness can vary by as much as 60% or more in a relatively homogeneous rock like Barre granite. This variation has been conclusively shown to be linked directly to the microstructural anisotropy present in the rock, as represented by its microcrack density distribution and its orientation with respect to fracture propagation direction in the fracture toughness test. A fracture propagating at right angles to the major set of microcracks yielded the highest fracture toughness value. Such fractures, in contrast to the fracture propagating parallel to the dominant microcracks, were characterized by increasing roughness, segmentation, and creation of wing cracks. All fractures issuing from the notch tip in the fracture toughness tests gave rise to significant fracture process zones (FPZ) surrounding the major crack. The microcrack density in FPZ was found to increase by a factor of two or more, compared to that of the prefractured state in both Barre and Lac du Bonnet granites. In both cases, the resulting microcracks in this zone were closely aligned with the major fracture plane. Real-time monitoring by AE evolution of the crack at the notch tip and that of FPZ

with time showed that AE rate increased exponentially until a few seconds before actual failure of the sample. Analysis showed that the dominant fracture mechanism during the prefailure state was due to tensile mode, whereas, in the post-failure state it was divided equally between tensile and shear modes. Out of plane deviation of the main fracture may explain increased shear-type AE events just prior to final rupture loaded under Mode I. The formation of FPZ and the major fracture plane could be accurately tracked through the detected AE events, and the results on FPZ width agreed very well with that of the direct microscopic analysis of the failed samples.

The study reported here is part of a continuing investigation on fracture behavior of rock under varying loads for a range of parameters. This includes understanding the relationship between *P*-wave velocity anisotropy and crack density, AE focal mechanism analysis using the moment tensor method, cumulative AE energy, amplitude and duration of load as well as temperature. Establishment of a relationship between fracture toughness and ultrasonic velocities, which could allow the estimation of material toughness by performing *P*- and *S*-velocity measurements, would be of very significant interest in future research. Measurement of fracture toughness under varying strain rates under dynamic loading conditions, and the effect of the latter on formation of the fracture process zone would further our understanding of the fracture process in rock.

#### REFERENCES

- CHELIDZE, T., REUSCHLE, T. and GUEGUEN, Y. (1994), *A theoretical investigation of the fracture energy of heterogeneous brittle materials*, J. Phys. Condens. Matter 6, 1857–1868.
- CHEN, Y., NISHIYAMA, T., KUSUDA, H., KITA, H. and SATO, T. (1999), *Correlation between microcrack distribution patterns and granite rock splitting planes*, Int J Rock Mech. Min Sci. 36, 535–541.
- DOUGLASS, P.M. and VOIGHT, B. (1969), *Anisotropy of granite: A reflection of microscopic fabric*, Geotechnique 19, 376–398.
- DWIVEDI, R.D., SONI, A.K., GOELL, R.K. and DUBE, A.K. (2000), *Fracture toughness of rock under subzero temperature conditions*, Int J Rock Mech. Min Sci. Geomech. Abstr. 30, 821–824.
- ENOKI, M. and KISHI, T. (1995), *Effect of rate on the fracture mechanism of TiAl*, Mat. Sci. Engin. A192/193, 420–426.
- HASHIDA, T. (1993), *Fracture toughness testing of core-based specimens by acoustic emission*, Int J Rock Mech. Min Sci. Geomech. Abstr. 30, 1, 61–69.
- IQBAL, M.J. and MOHANTY, B. (2005), *Fracture toughness measurement in brittle rocks*, Proc. 33rd Ann. Conf. Canadian Soc. Civil Engg., GC-220-1-7.
- ISRM (1988), *Suggested method for determining the fracture toughness of rocks*, Int J Rock Mech Min Sci Geomech Abstr. 25, 73–96.
- ISRM (1995), *Suggested method for determining Mode I fracture toughness using cracked Chevron notched Brazilian disc (CCNBD) specimens*, Int J Rock Mech. Min Sci. Geomech. Abstr. 32, 57–64.
- JANSSEN, C., WAGNER, F.C., ZANG, A. and DRESEN, G. (2001), *Fracture process zone in granite: A microstructural analysis*, Int. J. Earth Sci. 90, 46–59.
- KACHANOV, M. (1994), *Elastic solid with many cracks and related problems*, Adv. Appl. Mech. 30, 259–445.
- KEVIN, T. and O'BRIEN, (1998), *Interlamiar fracture toughness: the long and winding road to standardization*, composites, Part B 29B, 57–62.

- KIRBY, G.C. and MAZUR, C.J. (1985), *Fracture toughness testing of coal*, 26 US Symp. on rock mechanics, Rapid City, SD.
- KRANZ, R.L. (1983), *Microcrack in rocks: A review*, Tectonophysics 100, 449–480.
- LABUZ, J.F., SHAW, S.P. and DOWDING, C.H. (1987), *The fracture process zone in granite: Evidence and effect*, Int. J. R. Mech. Min. Sci. Geomech. Abstr. 24, 235–246.
- LAUNEAU, P. and ROBIN, P.-Y.F. (1996), *Fabric analysis using the intercept method*, Tectonophysics 267, 91–119.
- LEI, X., KUSUNOSE, K., RAO, M.V.M.S., NISHIZAWA, O. and SATOH, T. (2000), *Quasi-static fault growth and cracking in homogeneous brittle rock under triaxial compressive using acoustic emission monitoring*, J. Geophys. Res. 105, 6127–6139.
- LI, H.X. and XIAO, X.R. (1995), *An approach on the Mode-I fracture toughness anisotropy for materials with layered microstructures*, Engin. Fract. Mech. 52, 4, 671–683.
- LOCKNER, D. (1993), *The role of acoustic emission in the study of rock fracture*, Int. J. Rock Mech. Min. Sci. and Geomech. Abstr. 30, 7, 883–899.
- LOCKNER, D. E. (1996), *Brittle fracture as an analog to earthquakes: can acoustic emission be used to develop a viable prediction strategy*, J. Acous. Emission 14, 88–101.
- LOCKNER, D.E., BYERLEE, J.D., KUKSENKO, V., PONOMAREV, A. and SIDORIN, A. (1991), *Quasi-static fault growth and shear fracture energy in granite*, Nature 350, 39–42.
- LOCKNER, D.A. and MADDEN, T. R. (1991), *A Multiple-crack model of brittle fracture. Non-time-dependent simulation*, J Geophys. Res. 96, 19623–19643.
- MADDEN, T.H. (1983), *Microcrack Connectivity in Rocks: A renormalization group approach to the critical phenomena of conduction and failure in crystalline rocks*, J. Geophys. Res. 88, 585–592.
- MOORE, D.E. and LOCKNER D.A. (1995), *The role of microcracking in shear-fracture propagation in granite*, J Struct. Geol. 17, 95–114.
- NASSERI, M.H.B., MOHANTY, B. and PRASAD, U. (20002), *Investigation of micro-structural properties of selected rocks and their effect on fracture toughness*, NARMS, Toronto, Canada, 961–968.
- NASSERI, M.H.B. MOHANTY, B. and ROBIN, P.-Y.F. (2005a), *Characterization of microstructures and fracture toughness in five granitic rocks*, Int. J. Mech. Min. Sci. 42, 450–560.
- NASSERI, M.H.B., THOMPSON, B., SCHUBNEL, A. and YOUNG R.P. (2005b), *Acoustic emission monitoring of Mode I fracture toughness (CCNBD) test in Lac du Bonnet granite*, ARMA/USRMS, Alaska Rocks, (2005), Anchorage, Alaska, 05-741.
- NELDER, J. and MEAD, R. (1965), *A simplex method for function minimization*, Computer J. 7: 308–312.
- PRIKRYL, R. (2001), *Some micromechanical aspects of strength variation in rocks*, Int. J. Rock Mech. Min. Sci. 38, 671–682.
- SANO, O., KUDO, Y. and MIZUTA, Y. (1992), *Experimental determination of elastic constants of Oshima granite, Barre granite, and Chelmsford granite*, J. Geophys. Res. 97, B3, 3367–3379.
- SCHEDL, A., KRONENBERG, A.K. and TULLIS, J. (1986), *Deformation microstructures of Bare granite: An Optical SEM and TEM Study*, Tectonophysics 122, 149–164.
- SCHOLZ, C.H., DAWERS, N.H., YU, J.-Z. and ANDERS, M.H. (1993), *Fault growth and fault scaling laws: preliminary results*, J. Geophys. Res. 98, 21952–21961.
- TAKEMURA, T., GOLSHANI, A., ODA, M. and SUSUKI, K. (2003), *Preferred orientation of open microcracks in granite and their relation with anisotropic elasticity*, Int. J. Mech. Min. Sci. 40, 443–454.
- VERMILY, J.M. and SCHOLZ, C.H. (1999), *Fault propagation and segmentation: insight from the microstructural examination of a small fault*, J. Struct. Geology 21, 1623–1636.
- WILSON, J.E., CHESTER, J.S. and CHESTER, F.M. (2003), *Microcrack analysis of fault growth and wear processes, punchbowl fault, Sand Andreas System, California*, J. Struct. Geology 25, 1855–1873.
- YOUNG, R.P. and MARTIN, C.D. (1993), *Potential role of acoustic emission/microseismicity investigations in the site characterization and performance monitoring of nuclear waste repositories*, Int. J. Rock Mech. Min. Sci. 30, 797–803
- YOUNG, R.P., COLLINS, D.S., REYES-MONTES, J.M. and BAKER, C. (2004), *Quantification and interpretation of seismicity*, Int. J. Rock Mech. 41(8), 1317–1328.
- ZANG, A., WAGNER, C., STANCHITS, S., DRESEN, G., ANDRESEN, R. and HAIDEKKER, M.A. (1998), *Source analysis of acoustic emissions in aue granite cored under symmetric and asymmetric compressive loads*, J. Geophys. Res. 135, 1113–1130.

- ZANG, A. WAGNER, C.F., STANCHITS, S., JANSSEN, C. and DRESEN, G. (2000), *Fracture process zone in granite*, *J Geophys. R.* 105, B10, 23651–23661.
- ZIETLOW, W.K. and LABUZ, J.F. (1998), *Measurement of the intrinsic process zone in rock using acoustic emission*, *Int. J. R. Mech. Min. Sci.* 3, 291–299.

(Received May 22, 2005, revised September 28, 2005, accepted September 29, 2005)



To access this journal online:  
<http://www.birkhauser.ch>

---